NANO · MICRO small
www.small-journal.com

A New Family of Layered Metal-Organic Semiconductors: Cu/V-Organophosphonates

Patrik Tholen, Lukas Wagner, Jean G. A. Ruthes, Konrad Siemensmeyer, Thi Hai Yen Beglau, Dominik Muth, Yunus Zorlu, Mustafa Okutan, Jan Christoph Goldschmidt, Christoph Janiak, Volker Presser, Özgür Yavuzçetin,* and Gündoğ Yücesan**

Herein, we report the design and synthesis of a layered redox-active, antiferromagnetic metal organic semiconductor crystals with the chemical formula $[Cu(H_2O)_2V(\mu\text{-}O)(PPA)_2]$ (where PPA is phenylphosphonate). The crystal structure of $[Cu(H_2O)_2V(\mu\text{-}O)(PPA)_2]$ shows that the metal phosphonate layers are separated by phenyl groups of the phenyl phosphonate linker. Tauc plotting of diffuse reflectance spectra indicates that $[Cu(H_2O)_2V(\mu\text{-}O)(PPA)_2]$ has an indirect band gap of 2.19 eV. Photoluminescence (PL) spectra indicate a complex landscape of energy states with PL peaks at 1.8 and 2.2 eV. $[Cu(H_2O)_2V(\mu\text{-}O)(PPA)_2]$ has estimated hybrid ionic and electronic conductivity values between 0.13 and 0.6 S m^{-1}. Temperature-dependent magnetization measurements show that $[Cu(H_2O)_2V(\mu\text{-}O)(PPA)_2]$ exhibits short range antiferromagnetic order between Cu(II) and V(IV) ions. $[Cu(H_2O)_2V(\mu\text{-}O)(PPA)_2]$ is also photoluminescent with photoluminescence quantum yield of 0.02%. $[Cu(H_2O)_2V(\mu\text{-}O)(PPA)_2]$ shows high electrochemical, and thermal stability.

1. Introduction

Developing layered semiconductive materials has been one of science's most active research areas. Semiconductive layered materials can find a variety of essential applications, including light harvesting, optoelectronics, light emitting devices, transistors, electrodes in supercapacitors, and sensing.[1–9] Despite their widespread industrial applications, there is a limited number of layered semiconductor material families in the literature.[10] Most common layered semiconductors include transition metal dichalcogenides, Perovskites, metal oxides, MXenes, graphene, and phosphorene.[11–17] Recently, layered metal-organic frameworks (MOFs) constructed with planar ortho-diimine and quinoid linkers have emerged as novel layered

P. Tholen, G. Yücesan
Institut für Lebensmittelchemie und Toxikologie
Technische Universität Berlin
Gustav-Meyer-Allee 25, 13355 Berlin, Germany
E-mail: guendog.yuecesan@hhu.de

L. Wagner, D. Muth, J. C. Goldschmidt
Department of Physics
Philipps-University Marburg
Renthof 7, 35037 Marburg, Germany

J. G. A. Ruthes, V. Presser
INM—Leibniz Institute for New Materials
Campus D22, 66123 Saarbrücken, Germany
E-mail: volker.presser@leibniz-inm.de

J. G. A. Ruthes, V. Presser
Department of Materials Science and Engineering
Saarland University
66123, Campus D22 Saarbrücken, Germany

K. Siemensmeyer, C. Janiak
Institut Quantenphänomene in neuen Materialien
Helmholtz-Zentrum Berlin für Materialien und Energie
Hahn-Meitner-Platz 1, 14109 Berlin, Germany

T. H. Y. Beglau, G. Yücesan
Institut für Anorganische Chemie und Strukturchemie
Heinrich-Heine-Universität Düsseldorf
Universitätsstraße 1, 40225 Düsseldorf, Germany

Y. Zorlu
Department of Chemistry
Gebze Technical University
Kocaeli 41100, Turkey

M. Okutan
Institute of High Frequency and Quantum Electronics
University of Siegen
57068 Siegen, Germany

V. Presser
saarene - Saarland Center for Energy Materials and Sustainability
66123, Campus C42 Saarbrücken, Germany

Ö. Yavuzçetin
Department of Physics
University of Wisconsin-Whitewater
Whitewater, WI 53190, USA
E-mail: yavuzceo@uww.edu

The ORCID identification number(s) for the author(s) of this article can be found under https://doi.org/10.1002/smll.202304057

DOI: 10.1002/smll.202304057

microporous semiconductors with applications as electrode materials in supercapacitors or as electrocatalysts for water splitting.[2,18] Compared to other layered material families, MOFs provide much richer structural diversity due to the possibility of using a myriad of secondary building units (SBUs) and organic linkers to construct novel MOF structures.[19] MOFs can also contribute to the structural diversity and applications where semiconductors are needed for applications such as photoluminescence and optoelectronics.[20] Despite, rich structural chemistry of MOFs and their potential to form the largest family of semiconductors, there is still a very limited amount of semiconductive and photoluminescent MOFs in the literature.[10] The use of dense layered SBUs in MOFs might help to introduce semiconductive and magnetic properties. However, so far, there have been very few reports on semiconductive MOFs with layered SBUs.

Recently our group and Dincă's group reported two new 3D semiconductive MOFs with layered SBUs.[21,22] To better understand the role of layered SBUs in semiconductive MOFs and potentially use them as isolated layers of semiconductors or use them to create isoreticular semiconductive MOFs in the future, we have decided to design and synthesize an isolated layered-semiconductive SBU that could be potentially used as a precursor to synthesize semiconductive MOFs with layered SBUs in the future. Therefore, we fully characterize the properties of isolated layered SBUs in this work.

To synthesize an isolated layered-semiconductive SBU, we have chosen bimetallic copper/vanadium oxides as the model system. Bimetallic compounds provide richer metal oxide oligomerizations in two- or three-dimensions.[23,24] Hypothetically, they can produce isolated layered SBUs in the presence of monotopic organic ligands that have limited bridging capability to make 3D frameworks. Copper vanadates, such as $Cu_{11}V_6O_{26}$ and $Cu_2V_2O_7$ are already known to be oxide semiconductors in the literature, and they were used as photoanode materials for photoelectrochemical water oxidation, but both copper vanadates and copper vanadyls were not studied in MOF synthesis.[25–27] Both copper and vanadium ions can provide multiple redox states leading to interesting electronic properties. In this work, we used monotopic phenylphosphonic acid, which cannot bridge layered SBUs to form a 3D structure. Herein, we report the first-time synthesis of a thermally and electrochemically stable, semiconductive, photoluminescent, and antiferromagnetic layered Cu/V organophosphonate $[Cu(H_2O)_2V(\mu\text{-}O)(PPA)_2]$, which is composed of a layered copper(hydrate) vanadium(oxido) diphosphonate $\{Cu(H_2O)_2V(\mu\text{-}O)(O_3P)_2\}$ SBU decorated with phenyl groups. The structure of $[Cu(H_2O)_2V(\mu\text{-}O)(PPA)_2]$ was determined by single crystal X-ray diffraction (PPA = phenylphosphonate). $[Cu(H_2O)_2V(\mu\text{-}O)(PPA)_2]$ exhibited exceptional ionic conductivity, and Cu(II) and V(IV) ions were found to be antiferromagnetically coupled with short-range order at low temperatures. $[Cu(H_2O)_2V(\mu\text{-}O)(PPA)_2]$ has high thermal stability of up to 400 °C.

2. Results

2.1. Synthesis of $[Cu(H2O)2V(\mu\text{-}O)(PPA)_2]$

All chemicals were purchased from Aldrich, Alfa-Aesar, and used without further purification. $[Cu(H_2O)_2V(\mu\text{-}O)(PPA)_2]$ was synthesized using polytetrafluoroethylene-lined Parr acid digestion vessels at 150 °C with 0.129 g $CuSO_4$ $5H_2O$, 0.060 g Na_3VO_4 and 0.450 g phenylphosphonic acid in 10 mL of double-deionized H_2O. The tiny green needles of $[Cu(H_2O)_2V(\mu\text{-}O)(PPA)_2]$ were obtained in almost 100% yield based on Na_3VO_4. As seen in Figure S1, Supporting Information, green needles of $[Cu(H_2O)_2V(\mu\text{-}O)(PPA)_2]$ have been collected (see Figure S1, Supporting Information).

2.2. Crystal Structure Description

The compound, $[Cu(H_2O)_2V(\mu\text{-}O)(PPA)_2]$ is built from phenylphosphonate units and has a 2D infinite secondary building unit composed of tetragonal-bipyramidal Cu(II), octahedral V(IV), and phosphonate groups. The inorganic layer is composed of alternating chains of edge-sharing $\{Cu(H_2O)_2(O_2P\text{-})_2\}$ tetragonal bipyramids, with trans-positioned aqua ligands and of corner-sharing trans-μ-O bridging $\{V(\mu\text{-}O)_2(O_2P\text{-})_4\}$ octahedra (**Figure 1**a,b). These chains are connected by the fully deprotonated phenylphosphonate groups to form the layered $[Cu(H_2O)_2V(\mu\text{-}O)(PPA)_2]$ structure. Phenyl groups are decorating the layered SBU on both sides and apical positions of the tetragonal bipyramid of Cu(II).

2.3. Band-Gap Measurement

In order to assess the semiconductivity of $[Cu(H_2O)_2V(\mu\text{-}O)(PPA)_2]$, we generated the Tauc plot obtained from the diffuse reflectance spectra with hand-picked single crystals of $[Cu(H_2O)_2V(\mu\text{-}O)(PPA)_2]$ using Schimadzu 2600 UV–vis-NIR spectrometer.[28–30] The Tauc plotting of $[Cu(H_2O)_2V(\mu\text{-}O)(PPA)_2]$ indicated an indirect band gap of 2.19 eV, which is within the semiconductive regime (**Figure 2**). The absorption and diffuse reflectance spectrum of $[Cu(H_2O)_2V(\mu\text{-}O)(PPA)_2]$ can be seen in Figure S2A,B, Supporting Information. To further analyze the semiconductive properties of $[Cu(H_2O)_2V(\mu\text{-}O)(PPA)_2]$, we have performed electrical conductivity measurements, DC measurements and impedance spectroscopy.

2.4. Electrical Conductivity Measurements

Van der Pauw, two- or four-probe pellet methods are among the most common techniques of measuring electrical conductivity on MOFs.[31] However, these methods can introduce technical challenges like small contact areas and high contact resistances due to unmatched work functions. Small contact areas can also be a challenge while working with fragile crystals of reduced sample quantities. Other than supercapacitor or battery applications, MOFs can also serve in chemiresistive sensing fields,[32] which require 2D exposed areas with better electrical contact of the electrodes.[33] Gold interdigitated electrode (IDE) arrays are ideal platforms to exhibit not only intrinsic but also surface conducting mechanisms via chemicapacitive or chemiresistive properties.[34]

In this work, we have investigated the electrical properties of $[Cu(H_2O)_2V(\mu\text{-}O)(PPA)_2]$ using IDE arrays due to their

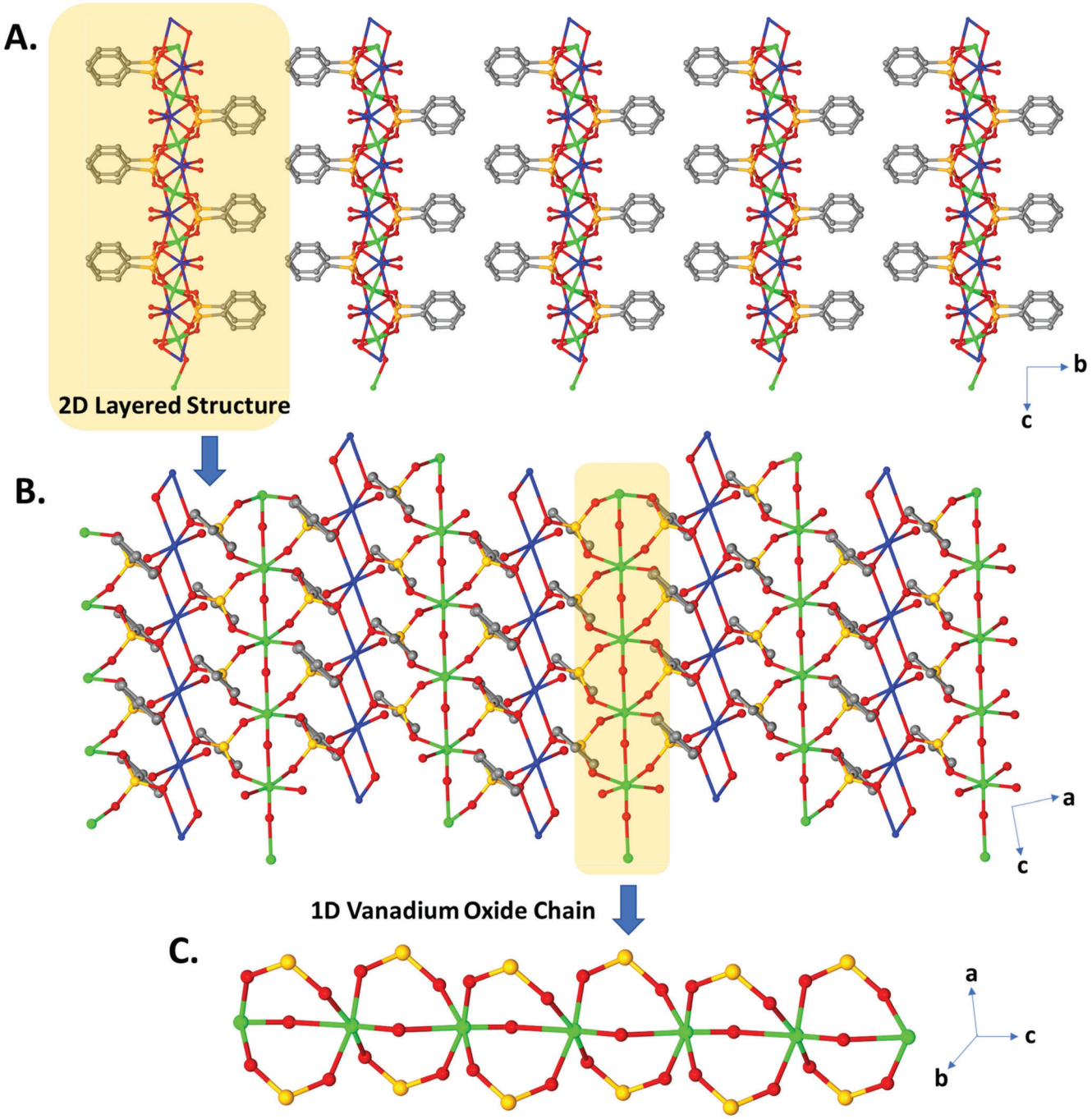

Figure 1. A) Side view of layered $[Cu(H_2O)_2V(\mu\text{-}O)(PPA)_2]$. B) Top view of layers and coordination environment of V(IV) and Cu(II) atoms in $[Cu(H_2O)_2V(\mu\text{-}O)(PPA)_2]$. C) A view of isolated alternating vanadium oxide chain (Color scheme: phosphorus – yellow, oxygen – red, copper – blue, vanadium – green, carbon – grey).

high direct current (DC) resistances. We randomly placed $[Cu(H_2O)_2V(\mu\text{-}O)(PPA)_2]$ crystals on IDE array produced by Muson R&E. Crystals were covered with a clear polycarbonate window and exerted 100 g of uniform force through a scale weight (Figure S3, Supporting Information provides a detailed description of IDE arrays and microscopy images). Although this method eliminates isotropic conduction pathway measurements of electrical conductivity, one can still measure bulk electrical properties of the sample. The in-air (ambient relative humidity at 21%), DC measurements of the sample gave a resistance of $\approx 10^{12}$ Ω with an estimated conductivity of $\approx 10^{-8}$ S m^{-1}, which could be due to the high contact resistance and associated unmatched work functions between the gold electrodes and the sample.

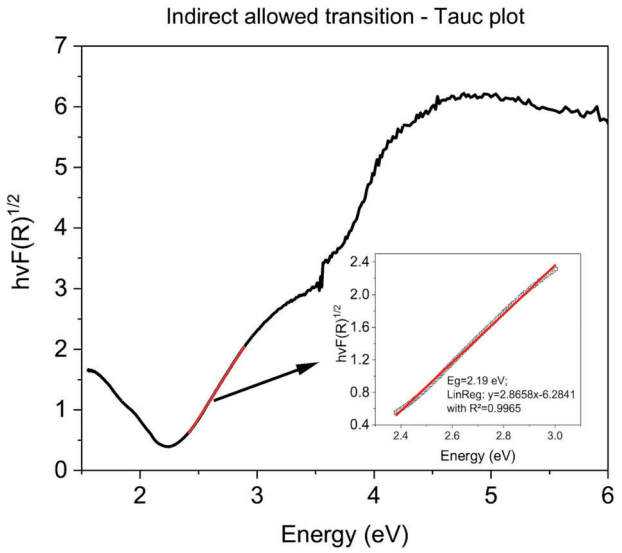

Figure 2. Tauc plotting of diffuse reflectance spectrum of $[Cu(H_2O)_2V(\mu\text{-}O)(PPA)_2]$.

2.4.1. DC Resistance of Hydrated Sample versus Mass of Absorbed Water

If MOF systems are designed for supercapacitor and battery applications, they require to be hydrated with other ionic electrolytes. In order to investigate the protonic/ionic conduction mechanisms, $[Cu(H_2O)_2V(\mu\text{-}O)(PPA)_2]$ sample on the IDE array was hydrated following a triple-rinsing process with pure water (Figure S2, Supporting Information). The purpose of the rinsing process is to remove residual ionic impurities due to the synthesis process. Following rinsing, the sample was pressed against the IDE array using the clear polycarbonate window to increase surface area of the contact points of electrodes and the sample. The polycarbonate window was removed and pure water was dropped onto the IDE array through a pipette where the sample resided. The IDE array was taped on a digital micro balance with sliding doors (Adventurer, OHAUS) to measure the amount of water absorbed by the sample. For electrical conductivity measurements, PTFE coated, 24 AWG multi-strand wires were soldered to the IDE array to minimize strain. Both AC and DC electrical measurements were performed, and the amount of absorbed water was recorded with 15–20 min of time intervals. For DC measurements, we programmed our SourceMeter to sweep between ±100 mV and the DC resistance values are calculated from the linear fittings (**Figure 3**)

As expected, the DC resistance of the sample increases as the water evaporates. When all the water evaporated, we measured DC resistances on the order of 10^{12} Ω similar to the in-air measurements (not shown in Figure 3 due to scaling). For the first few data points, the DC resistance stabilizes ≈ 85 kΩ and then gradually increases. This stabilization period could be due to the absorption and the saturation of water inside the $[Cu(H_2O)_2V(\mu\text{-}O)(PPA)_2]$. SourceMeter was programmed to sweep between ±100 mV, and the IV measurements were recorded with 15–30 min of time intervals (Figure S5, Supporting Information). We used the least squares fit for each sweep and calculated the DC resistance values (Figure S6, Supporting Information). In order to find the relation between the DC resistance value versus amount of water on the sample, the data points with reduced absorbed water on the sample were used resulting in smaller standard deviations.

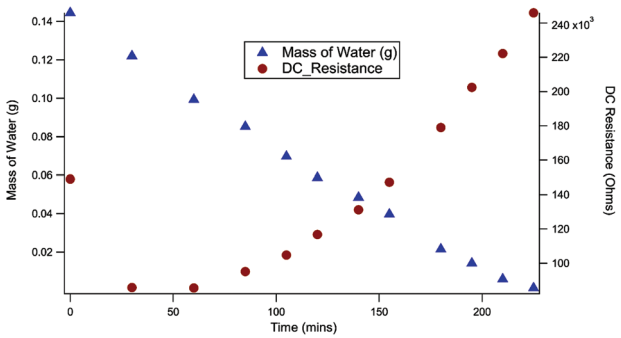

Figure 3. DC resistance of the $[Cu(H_2O)_2V(\mu\text{-}O)(PPA)_2]$ sample on IDE array versus the mass of water remaining on the sample. The data points for DC resistance were calculated from the IV sweeps of the sample.

$$R_{DC} = R_{DC-0} + Am^n \quad (1)$$

Here, R_{DC-0} is the offset of the DC resistance (2.60 ± 0.05)10^5 Ω, A is (−7.9 ± 0.9)10^5 Ω, m is the amount of water on the sample in grams, and $n = 0.60 \pm 0.05$. Based on this relation, if the mass of water is reduced, which is the case of dehydration of the sample, the equation converges to DC resistance of (2.60 ± 0.05)10^5 Ω. The DC resistance would involve bulk resistance of the sample, blocking electrode potentials (contact resistance) and also the double layer capacitance.

(Supporting Information provides details on the estimation of effective conductance and experimental DC resistance values of blank IDE Array with standard solutions). The DC conductivity of DI water used in these experiments were estimated to be 2.6×10^{-6} S m^{-1}, which is ≈5000 times more conductive than standard DI water.

2.4.2. AC Conductivity Measurements of Hydrated Sample versus Mass of Absorbed Water

Impedance measurements were carried out using Analog Discovery 2 module with impedance analyzer (Digilent Inc.) at frequencies between 1 kHz and 1 MHz with an applied signal of 100 mV RMS. We measured a blank (no sample) IDE array with standard conductivity solutions and with pure water for calibration purposes (Figure S8, Supporting Information). Using a circuit model,[35] with Warburg element (Figure S9, Supporting Information), R_{lead} and R_g are the lead and geometrical resistances, C_{dl} and C_g are the double-layer and geometrical capacitances, respectively.

Z_W is the Warburg diffusion impedance element (showing up as 45° line on the Nyquist plots with lower frequencies) in series with geometrical resistance. Since our system consists of a periodic pattern of electrodes, R_g also involves the solution resistance. In our model, at higher frequencies, the reactance values of both capacitors and Warburg element would get insignificant, leaving only the lead and the solution resistances in series.

This is why for higher conductivity solutions with higher frequencies, the overall impedance value of the system approaches to lead resistance which is consistent with our DC measurements (<20 Ω). Our LCR measurements indicate that C_g is in the order of 10 pF when it is blank. For frequency sweeps between 1 kHz and 1 MHz, this corresponds to the reactance values between 10^7 and 10^4 Ω, respectively. The AC measurements of the hydrated sample as a function of the reduced mass of absorbed water are shown in Figure S10, Supporting Information. For gold electrodes with water electrolyte, the anodic and cathodic potential limits V (versus NHE), are 1.53 and −0.32 V, respectively,[36] therefore faradaic currents cannot be detected since our excitation potential is below 100 mV. Due to the metal-electrolyte-metal system, it is possible to have a double layer capacitance on the order of 10–50 μF cm^{-2} due to the diffuse region of ionic species.[37]

When the water is absorbed by the $[Cu(H_2O)_2V(\mu\text{-}O)(PPA)_2]$ structure, the system exhibits double hooks and semi-circles in high and low frequency regions. Here the matrix behaves as a mixed conducting thin film with both ionic/electronic and protonic currents competing. The ions and electrons at the interface influence the charge transport mechanism, which in result gives two different time constants, protonic and electronic/ionic transport.[38] As water depletes, the high-frequency region semi-circle starts shrinking, indicating a reduction in the electronic/ionic conduction (Figure S10, Supporting Information, left). After 120 min, the water remaining in the matrix only transports protonic conduction corresponding to the low frequency semi-circle. After 240 minutes (Figure S10, Supporting Information, middle), as all the water evaporates, protonic conduction is lost too, and the system behaves like an in-series constant phase element (CPE) with its impedance converging toward the lead resistance.[39] This aligns with the mass measurements and the DC resistance measurements. The improved circuit model with $[Cu(H_2O)_2V(\mu\text{-}O)(PPA)_2]$ sample on the IDE array would involve two Warburg impedances with different Warburg coefficients (Figure S11, Supporting Information). The circuit elements with superscripted index "e" and "p" correspond to electronic and protonic/ionic conductivities.

We can estimate the electronic and protonic resistance values (R_g), using the Nyquist plots (Figure S10, Supporting Information). Since the reactance value of C_g is more significant than 10^4 Ω, and the lead resistance R_{lead} is lower than 20 Ω, they can be neglected compared to lower impedances R_g. Using semi-circle approximation for RC circuits, the R_g values for electron transport shift from 450 to 100 Ω. After 120 min, the electronic transport is dominated by protonic transport which is between 300 and 450 Ω, until the sample is fully dehydrated after 240 min. Using Equation (1) for conductivity calculations, I/V is $(\approx 100\text{–}450\ \Omega)^{-1}$, $L = 90$ μm, $N_e \approx 10$, $t \approx 30$ μm, $w_e \approx 5$ mm which gives an estimated bulk conductivity range of ≈0.13–0.60 S m^{-1}.

2.5. Photoluminescence

Figure 4a shows the absorptance spectra and photoluminescence spectra for excitation with a 380 nm laser of a crystal powder sample. As seen in the complementary measurement displayed in Figure 4B, the absorptance spectrum displays an unexpected rise for wavelengths above ≈550 nm. For a classical semiconductor, one would expect a decrease of absorptance at the band gap, whereas the absorptance should ideally be zero for higher wavelengths. The bandgap determined from the Tauc plot in Figure 2 of 2.19 eV (566 nm) corresponds well to the observed PL spectrum with a broad peak at around the same wavelength. The PL spectrum displays a more than three times higher second peak at a peak wavelength of 690 nm (1.80 eV). This shows that there is a more favorable channel for radiative recombination at this lower band energy.

We performed a second measurement on a separate measurement setup to measure the photoluminescence spectrum for excitation with a 632 nm laser. Although the excitation energy is close to or below the bandgap (absorbance 11.3%), the sample was still weakly luminescent with a PL quantum yield of ≈0.02%. As displayed in Figure 4B (blue line), for this excitation energy, two peaks can still be recognized, but here, they display the same PL intensity. Overall, the investigations reveal a complex and interesting landscape of energy states requiring further investigation.

2.6. Magnetic Properties

Magnetization measurements were carried out using a commercial Squid magnetometer (Quantum Design MPMS3) in an applied field up to 7 T in a temperature range between 2 and 400 K. The sample was filled into a plastic capsule provided by the

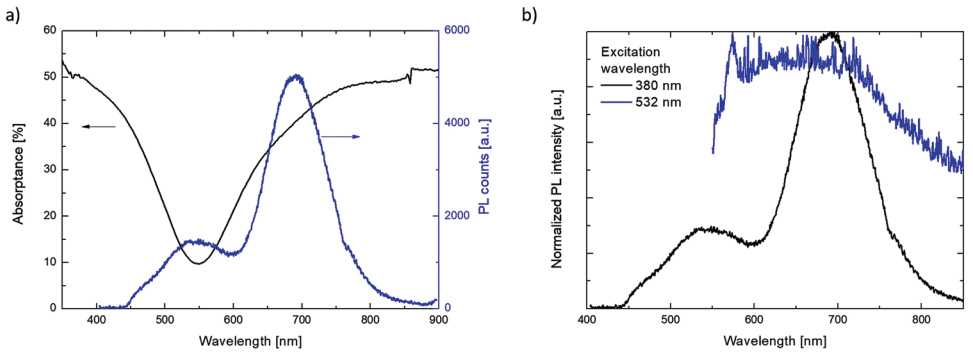

Figure 4. a) Absorbance spectrum (black, left axis) and photoluminescence spectrum for an excitation at 380 nm (blue, right axis). b) Comparison of normalized photoluminescence intensity spectra for excitation with 380 (black) and 632 nm (blue).

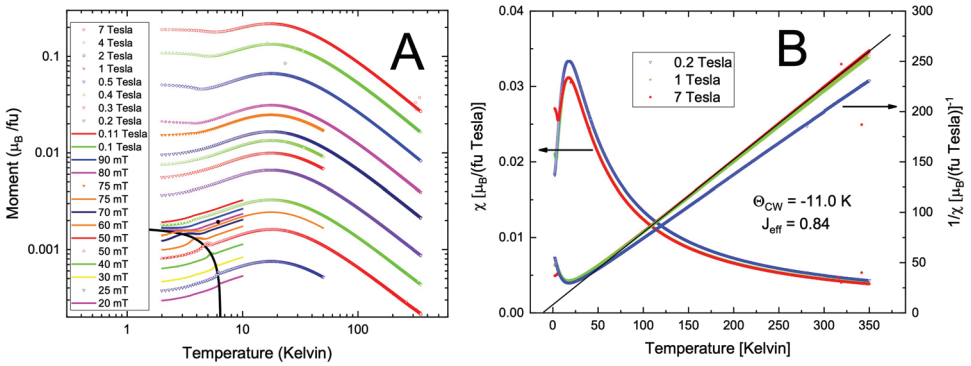

Figure 5. A) Magnetization of [Cu(H2O)2V(μ-O)(PPA)2] as a function of magnetic field and temperature. B) Susceptibility and its inverse for a selection of field values. For both, A and B, the signal is given in μB for one formula unit [fu]. The solid black line in A is a calculated phase boundary with parameters given in the text. The black solid line in B shows the Curie–Weiss fit obtained on the 7 T data set.

manufacturer of the instrument. The sample mass was 3.74 mg. For simplicity the data are referred to one magnetic ion per formula unit assuming a gyromagnetic ratio g = 2. The magnetization data are shown in **Figure 5**a. The maximum of the magnetization is observed at $T = 18$ K. Up to 7 Ta, this maximum is not affected by the magnetic field. Below $T = 7$ K, the magnetic behavior gets more complex. In low fields, a sharp kink is observed, and the field dependence is well described by a mean field phase boundary given by $1 = (B/B_c)^2 + (T/T_c)^2$ with $B_c = 90\ mT$ and $T_c = 6.4$ K. In the higher field, the low-temperature magnetization shows paramagnetic behavior, it increases with decreasing temperature. At the highest field of 7 T, saturation is observed.

The susceptibility confirms the independence of the magnetization maximum at 18 K on the magnetic field for large field values. The inverse susceptibility (Figure 5) shows a decrease in slope in low fields, which may be attributed to a small ferromagnetic impurity. For a Curie Weiss fit the 7 Tesla data set was used because there the impact of an impurity is expected to be negligible. It gives an effective angular momentum of J = 0.84 and a Curie Weiss temperature of $\theta_{CW} = -11\ K$.

Some conclusions concerning the magnetism of $[Cu(H_2O)_2V(\mu\text{-}O)(PPA)_2]$ are possible. The effective angular momentum of $J = 0.84$ is much larger than the S = ½ momentum expected when only the Cu ions carry a magnetic moment. Looking at the chemical composition of $[Cu(H_2O)_2V(\mu\text{-}O)(PPA)_2]$ – C_{12} H_{18} Cu O_9 P_2 V – there is in addition the unpaired electron of the V(IV) ions, they can carry a magnetic moment as well. Both the Cu and the V ions reside on parallel chains along the crystallographic c-axis. Along the chain the Cu ions are linked by two oxygen atoms and the V ions have a direct link only by one oxygen atom. Thus, the magnetic behavior of Cu- and V-chains can be different. The broad maximum of the susceptibility at 18 K likely results from short-range order along the chains. It is not possible to say which ion-chain is responsible for short-range order, it could as well be both.

Similarly, it is impossible to assign the ordering observed at low temperatures in a low field to one of the potential magnetic species. The observed Curie–Weiss temperature, however, appears quite consistent with the characteristic temperatures of the observed magnetic features and indicates dominant antiferromagnetic interactions. In summary, $[Cu(H_2O)_2V(\mu\text{-}O)(PPA)_2]$ shows complex magnetic behavior based on the presence of Cu- and V-ions in this material. More detailed information requires element-selective methods, for example, using synchrotron radiation.

2.7. Thermal Stability

$[Cu(H_2O)_2V(\mu\text{-}O)(PPA)_2]$ was synthesized under hydrothermal reaction conditions at 150 °C and under autogenous pressure. We characterized the thermal stability of $[Cu(H_2O)_2V(\mu\text{-}O)(PPA)_2]$ under N_2 flow at a temperature ramp rate of 10 °C min^{-1} from room temperature until 900 °C. TGA results in Figure S12, Supporting Information, indicated 7.1% mass loss between 100 and 150 °C, which indicates the evaporation of two copper-coordinated water molecules. This weight loss matches perfectly with the calculated 7.1% mass loss. 22.5% weight loss at ≈400 °C indicates that the organic components of PPA (C_6H_5) has started to decompose (calculated 26.9%). The decomposition of the remaining 4.4% PPA units continues slowly until ≈800 °C. Residual mass correspond to $CuV(PO_4)_2$.

2.8. Electrochemical Stability

The electrochemical stability of $[Cu(H_2O)_2V(\mu\text{-}O)(PPA)_2]$ was investigated using cyclic voltammetry, galvanostatic charge-discharge, and electrochemical impedance analysis in both aqueous and organic electrolytes. Supporting information S15 and S16 presents all details and results. The material demonstrated electrochemical stability, with no signs of irreversible reactions. Also, it exhibited superior performance in an organic half-cell compared to aqueous, as evidenced by higher specific current. Figure 3A elucidated the electrochemical behavior with two CV cycles, where the first cycle showed the formation of a solid electrolyte interface (SEI) in the potential window of 0.1–0.3 V versus Li/Li^+ and subsequent copper oxide formation and lithiation: at 1.21 V ($Cu_{1-x}{}^{II}Cu_{1-x}{}^{I}O_{1-x/2} \rightarrow Cu_2O$) and 1.49 V ($Cu_2O \rightarrow Li_2O$).[40,41] However, the second cycle displayed lower current values, indicating irreversible SEI formation, though the material still underwent lithiation and de-lithiation. The same behavior was observed in higher scan rates which are presented in FigureS14A, Supporting Information.

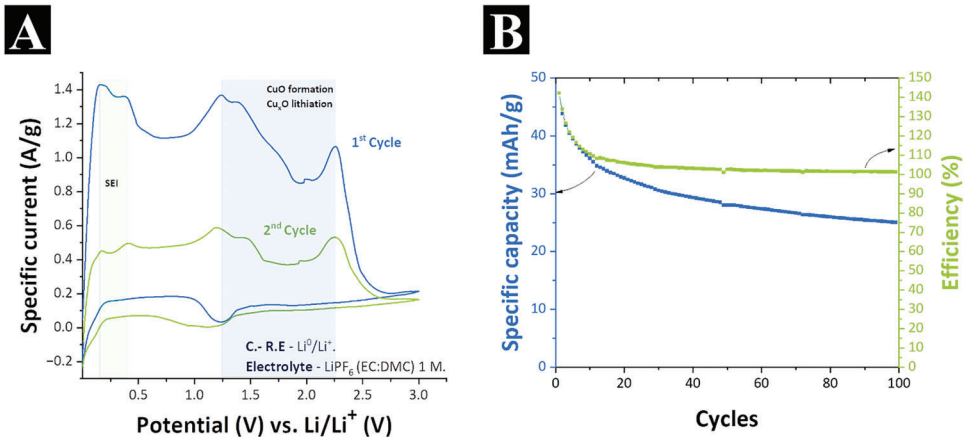

Figure 6. Electrochemical characterization $[Cu(H_2O)_2V(\mu\text{-}O)(PPA)_2]$ in organic electrolyte $LiPF_6$ 1 M in EC:DMC (1:1) versus Li/Li^+ as reference and counter-electrode. A) Cyclic voltammogram at 0.1 mV s^{-1}. B) Galvanostatic cycling with potential limitation at 100 mA g^{-1} for 100 cycles.

To further understand the electrochemical behavior and stability of $[Cu(H_2O)_2V(\mu\text{-}O)(PPA)_2]$, 100 cycles of GCPL were conducted at a specific current of 100 mA g^{-1} and are presented in FigureS14B, Supporting Information. **Figure 6**B shows that the specific capacity values were not comparable to state-of-the-art materials, nevertheless, the material exhibited stable efficiency, suggesting its stability during redox processes in organic electrolytes.

3. Conclusions

Herein, we report a new family of layered semiconductive, antiferromagnetic and photoluminescent metal organic compound $[Cu(H_2O)_2V(\mu\text{-}O)(PPA)_2]$. it has collected 5 exceptional characteristics of electrical/ionic conductivity, semiconductivity, short range antiferromagnetic order, photoluminescence and stability (chemical, electrochemical and thermal) on the same platform. $[Cu(H_2O)_2V(\mu\text{-}O)(PPA)_2]$ exhibit high ionic/electrical conductivity between 0.13 and 0.60 S m^{-1}. Although, its specific capacity of 160 mAh g^{-1} in the first cycle is not comparable to the state-of-art, electrochemical data suggests a rare observed rapid stability in organic media, due to the formation SEI layer that protects the bulk material without hindering the lithiation process. Therefore, $[Cu(H_2O)_2V(\mu\text{-}O)(PPA)_2]$ family of compounds provide rich potential to produce stable Li+ ion batteries in the future. Its synthesis at 150 °C under autogenous pressure at pH 1.5 proves that $[Cu(H_2O)_2V(\mu\text{-}O)(PPA)_2]$ is a stable compound in water and acidic conditions. Furthermore, TGA indicates that $[Cu(H_2O)_2V(\mu\text{-}O)(PPA)_2]$ organic components starts to decompose at 400 °C. $[Cu(H_2O)_2V(\mu\text{-}O)(PPA)_2]$. Our result indicates that layered Cu/V/P/O-based metal organic semiconductors can perform diverse applications ranging from optoelectronics to energy storage systems. Due to the rich structural diversity and plethora of phosphonate metal oxide oligomerizations, thousands of new compounds of this family can be produced in near future to optimize the above-mentioned applications. Furthermore, such stable $[Cu(H_2O)_2V(\mu\text{-}O)(PPA)_2]$ building units can be hypothetically used as layered SBUs to generate semiconductive and magnetic MOFs, and they can be extended into porous MOFs via post synthetic modifications or using bridging linkers such as 1,4-phenyldiphosphonic acid, 4,4-biphenlydiphosphonic acid, and their longer tethered versions. We are currently working on this hypothesis to generate microporous 3D MOFs with layered SBUs such as $[Cu(H_2O)_2V(\mu\text{-}O)(PPA)_2]$.

[CCDC 2 257 417 contains the supplementary crystallographic data for this paper. These data can be obtained free of charge from The Cambridge Crystallographic Data Centre via www.ccdc.cam.ac.uk/data_request/cif.]

Supporting Information

Supporting Information is available from the Wiley Online Library or from the author.

Acknowledgements

P.T., L.W., and J.R. contributed equally to this work. G.Y. acknowledges funding from the German Research Foundation (YU-267/2). J.G.A.R. and V.P. acknowledge funding from the German Research Foundation (PR-1173/29). [Correction added after publication 22 November 2023: Affiliations were corrected.]

Open access funding enabled and organized by Projekt DEAL.

Conflict of Interest

The authors declare no conflict of interest.

Data Availability Statement

The data that support the findings of this study are available in the supplementary material of this article.

Keywords

layered magnetic materials, layered metal organic semiconductors, metal organic frameworks

Received: May 15, 2023
Revised: July 10, 2023
Published online: July 25, 2023

[1] D. Y. Lee, I. Lim, C. Y. Shin, S. A. Patil, W. Lee, N. K. Shrestha, J. K. Lee, S. H. Han, *J. Mater. Chem. A* **2015**, *3*, 22669.
[2] Q. H. Wang, K. Kalantar-Zadeh, A. Kis, J. N. Coleman, M. S. Strano, *Nat. Nanotechnol.* **2012**, *7*, 699.
[3] M. Gutiérrez, C. Martín, M. Van der Auweraer, J. Hofkens, J.-C. Tan, *Adv. Opt. Mater.* **2020**, *8*, 2000670.
[4] H. H. Hsu, C. Y. Chang, C. H. Cheng, S. H. Chiou, C. H. Huang, *IEEE Electron Device Lett.* **2014**, *35*, 87.
[5] Y. Liu, H. Zhou, N. O. Weiss, Y. Huang, X. Duan, *ACS Nano* **2015**, *9*, 11102.
[6] B. Sun, C. H. Zhu, Y. Liu, C. Wang, L. J. Wan, D. Wang, *Chem. Mater.* **2017**, *29*, 4367.
[7] D. Sheberla, J. C. Bachman, J. S. Elias, C. J. Sun, Y. Shao-Horn, M. Dinca, *Nat. Mater.* **2017**, *16*, 220.
[8] T. Chen, J. H. Dou, L. Yang, C. Sun, N. J. Libretto, G. Skorupskii, J. T. Miller, M. Dincă, *J. Am. Chem. Soc.* **2020**, *142*, 12367.
[9] M. G. Campbell, D. Sheberla, S. F., Liu, T. M. Swager, M. Dincă, *Angew. Chem., Int. Ed.* **2015**, *54*, 4349.
[10] L. S. Xie, G. Skorupskii, M. Dincă, *Chem. Rev.* **2020**, *120*, 8536.
[11] Z. Ling, C. E. Ren, M. Q. Zhao, J. Yang, J. M. Giammarco, J. Qiu, M. W. Barsoum, Y. Gogotsi, *Proc. Natl. Acad. Sci. USA* **2014**, *111*, 16676.
[12] M. Q. Zhao, C. E. Ren, Z. Ling, M. R. Lukatskaya, C. Zhang, K. L. Van Aken, M. W. Barsoum, Y. Gogotsi, *Adv. Mater.* **2015**, *27*, 339.
[13] M. F. El-Kady, Y. Shao, R. B. Kaner, *Nat. Rev. Mater.* **2016**, *1*, 16033.
[14] W. Li, Z. Wang, F. Deschler, S. Gao, R. H. Friend, A. K. Cheetham, *Nat. Rev. Mater.* **2017**, *2*, 16099.
[15] K. L. Hu, M. Kurmoo, Z. Wang, S. Gao, *Chemistry* **2009**, *15*, 12050.
[16] H. Xiao, Z.-S. Wu, L. Chen, F. Zhou, S. Zheng, W. Ren, H.-M. Cheng, X. Bao, *ACS Nano* **2017**, *11*, 7284.
[17] J. Sun, H. W. Lee, M. Pasta, H. Yuan, G. Zheng, Y. Sun, Y. Li, Y. Cui, *Nat. Nanotechnol.* **2015**, *10*, 980.
[18] S.-K. Su, C.-P. Chuu, M.-Y. Li, C.-C. Cheng, H. S. P. Wong, L.-J. Li, *Small Struct.* **2021**, *2*, 2000103.
[19] H. C. Zhou, J. R. Long, O. M. Yaghi, *Chem. Rev.* **2012**, *112*, 673.
[20] Y. Zorlu, L. Wagner, P. Tholen, M. M. Ayhan, C. Bayraktar, G. Hanna, A. O. Yazaydin, Ö. Yavuzçetin, G. Yücesan, *Adv. Opt. Mater.* **2022**, *10*, 2200213.
[21] C. A. Peeples, D. Kober, F.-J. Schmitt, P. Tholen, K. Siemensmeyer, Q. Halldorson, B. Çoşut, A. Gurlo, A. O. Yazaydin, G. Hanna, G. Yucesan, *Adv. Funct. Mater.* **2021**, *31*, 2007294.
[22] S. Kampouri, M. Zhang, T. Chen, J. J. Oppenheim, A. C. Brown, M. T. Payne, J. L. Andrews, J. Sun, M. Dincă, *Angew. Chem., Int. Ed.* **2022**, *61*, e202213960.
[23] A. Bulut, M. Wörle, Y. Zorlu, E. Kirpi, H. Kurt, J. Zubieta, S. Grabowsky, J. Beckmann, G. Yücesan, *Acta Crystallogr.,Sect. B: Struct. Sci.* **2017**, *73*, 296.
[24] G. Yucesan, M. H. Yu, W. Ouellette, C. J. O'Connor, J. Zubieta, *CrystEngComm* **2005**, *7*, 480.
[25] S. Gupta, Y. P. Yadava, R. A. Singh, *Z. Phys. B: Condens. Matter* **1987**, *67*, 179.
[26] M. K. Hossain, H. P. Sarker, P. Sotelo, U. Dang, I. Rodríguez-Gutiérrez, J. Blawat, A. Vali, W. Xie, G. Oskam, M. N. Huda, R. T. Macaluso, K. Rajeshwar, *Chem. Mater.* **2020**, *32*, 6247.
[27] L. Zhou, Q. Yan, J. Yu, R. J. R. Jones, N. Becerra-Stasiewicz, S. K. Suram, A. Shinde, D. Guevarra, J. B. Neaton, K. A. Persson, J. M. Gregoire, *Phys. Chem. Chem. Phys.* **2016**, *18*, 9349.
[28] B. D. Viezbicke, S. Patel, B. E. Davis, D. P. Birnie Iii, *Phys. Status Solidi* **2015**, *252*, 1700.
[29] J. Tauc, *Mater. Res. Bull.* **1968**, *3*, 37.
[30] J. Tauc, R. Grigorovici, A. Vancu, *Phys. Status Solidi* **1966**, *15*, 627.
[31] L. Sun, M. G. Campbell, M. Dincă, *Angew. Chem., Int. Ed. Engl.* **2016**, *55*, 3566.
[32] Z. Meng, A. Aykanat, K. A. Mirica, *J. Am. Chem. Soc.* **2019**, *141*, 2046.
[33] W. T. Koo, J. S. Jang, I. D. Kim, *Chem* **2019**, *5*, 1938.
[34] M. G. Campbell, M. Dincă, *Sensors* **2017**, *17*, 1108.
[35] N. F. Sheppard, R. C. Tucker, C. Wu, *Anal. Chem.* **1993**, *65*, 1199.
[36] S. R. Waldvogel, A. Kirste, S. Mentizi *Use of Diamond Films in Organic Electrosynthesis, Synthetic Diamond Films*, Wiley, Hoboken, NJ, **2011**, pp. 483–510.
[37] M. E. Orazem, B. Tribollet, *Electrochemical Impedance Spectroscopy*, John Wiley & Sons, New Jersey **2008**.
[38] D. Klotz, *Electrochem. Commun.* **2019**, *98*, 58.
[39] C. M. A. Brett, *Molecules* **2022**, *27*, 1497.
[40] S. Menkin, C. A. O'Keefe, A. B. Gunnarsdóttir, S. Dey, F. M. Pesci, Z. Shen, A. Aguadero, C. P. Grey, *J. Phys. Chem. C* **2021**, *125*, 16719.
[41] Y. Tan, Z. Jia, J. Sun, Y. Wasng, Z. Cui, X. Guo, *J. Mater. Chem. A* **2017**, *5*, 24139.